Chip based common-path optical coherence tomography system with an on-chip microlens and multi-reference suppression algorithm

Lantian Chang,[1,2,*] Nicolás Weiss,[3] Ton G. van Leeuwen,[3] Markus Pollnau,[4] René M. de Ridder,[5] Kerstin Wörhoff,[6] Vinod Subramaniam,[1,2,7] and Johannes S. Kanger[1,2]

[1]*Nanobiophysics, MESA + Institute for Nanotechnology, University of Twente, 7500 AE Enschede, The Netherlands*
[2]*MIRA Institute for Biomedical Technology and Technical Medicine, University of Twente, 7500 AE Enschede, The Netherlands*
[3]*Biomedical Engineering & Physics, Academic Medical Center, University of Amsterdam, 1100 DE Amsterdam, The Netherlands*
[4]*Department of Materials and Nano Physics, School of Information and Communication Technology, KTH - Royal Institute of Technology Isafjordsgatan, 22, SE-164 40 Kista, Sweden*
[5]*Faculty of Electrical Engineering, Mathematics and Computer Science, University of Twente, 7500 AE Enschede, The Netherlands*
[6]*LioniX BV, 7500 AL Enschede, The Netherlands*
[7]*Vrije Universiteit Amsterdam, De Boelelaan 1105, 1081 HV Amsterdam, The Netherlands*
**l.chang@utwente.nl*

Abstract: We demonstrate an integrated optical probe including an on-chip microlens for a common-path swept-source optical coherence tomography system. This common-path design uses the end facet of the silicon oxynitride waveguide as the reference plane, thus eliminating the need of a space-consuming and dispersive on-chip loop reference arm, thereby obviating the need for dispersion compensation. The on-chip micro-ball lens eliminates the need of external optical elements for coupling the light between the chip and the sample. The use of this lens leads to a signal enhancement up to 37 dB compared to the chip without a lens. The light source, the common-path arm and the detector are connected by a symmetric Y junction having a wavelength independent splitting ratio (50/50) over a much larger bandwidth than can be obtained with a directional coupler. The signal-to-noise ratio of the system was measured to be 71 dB with 2.6 mW of power on a mirror sample at a distance of 0.3 mm from the waveguide end facet. Cross-sectional OCT images of a layered optical phantom sample are demonstrated with our system. A method, based on an extended Fourier-domain OCT model, for suppressing ghost images caused by additional parasitic reference planes is experimentally demonstrated.

OCIS codes: (130.0130) Integrated optics; (130.3120) Integrated optics devices; (130.3990) Micro-optical devices; (110.4500) Optical coherence tomography; (100.1830) Deconvolution.

References and links

1. D. Huang, E. A. Swanson, C. P. Lin, J. S. Schuman, W. G. Stinson, W. Chang, M. R. Hee, T. Flotte, K. Gregory, C. A. Puliafito, and J. G. Fujimoto, "Optical coherence tomography," Science **254**(5035), 1178–1181 (1991).
2. W. Drexler and J. G. Fujimoto, *Optical Coherence Tomography: Technology and Applications* (Springer-Verlag, 2008).
3. M. Wojtkowski, "High-speed optical coherence tomography: basics and applications," Appl. Opt. **49**(16), D30–D61 (2010).
4. M. Dufour, G. Lamouche, B. Gauthier, C. Padioleau, and J.-P. Monchalin, "Inspection of hard-to-reach industrial parts using small-diameter probes," Proc. SPIE **6343**, 63431Z (2006).
5. G. Song and K. Harding, "OCT for industrial applications," Proc. SPIE **8563**, 85630N (2012).

#261809 Received 28 Mar 2016; revised 1 May 2016; accepted 2 May 2016; published 1 Jun 2016

6. W. J. Walecki, K. Lai, A. Pravdivtsev, V. Souchkov, P. Van, T. Azfar, T. Wong, S. H. Lau, and A. Koo, "Low-coherence interferometric absolute distance gauge for study of MEMS structures," Proc. SPIE **5716**, 182–188 (2005).
7. W. J. Walecki, K. Lai, V. Souchkov, P. Van, S. H. Lau, and A. Koo, "Novel noncontact thickness metrology for backend manufacturing of wide bandgap light emitting devices," Phys. Status Solidi, C Conf. Crit. Rev. **2**(3), 984–989 (2005).
8. D. Stifter, "Beyond biomedicine: a review of alternative applications and developments for optical coherence tomography," Appl. Phys. B **88**(3), 337–357 (2007).
9. A. F. Fercher, "Optical coherence tomography - development, principles, applications," Z. Med. Phys. **20**(4), 251–276 (2010).
10. M. Choma, M. Sarunic, C. Yang, and J. Izatt, "Sensitivity advantage of swept source and Fourier domain optical coherence tomography," Opt. Express **11**(18), 2183–2189 (2003).
11. B. I. Akca, B. Považay, A. Alex, K. Wörhoff, R. M. de Ridder, W. Drexler, and M. Pollnau, "Miniature spectrometer and beam splitter for an optical coherence tomography on a silicon chip," Opt. Express **21**(14), 16648–16656 (2013).
12. V. D. Nguyen, N. Weiss, W. Beeker, M. Hoekman, A. Leinse, R. G. Heideman, T. G. van Leeuwen, and J. Kalkman, "Integrated-optics-based swept-source optical coherence tomography," Opt. Lett. **37**(23), 4820–4822 (2012).
13. G. Yurtsever, B. Považay, A. Alex, B. Zabihian, W. Drexler, and R. Baets, "Photonic integrated Mach-Zehnder interferometer with an on-chip reference arm for optical coherence tomography," Biomed. Opt. Express **5**(4), 1050–1061 (2014).
14. G. Yurtsever, N. Weiss, J. Kalkman, T. G. van Leeuwen, and R. Baets, "Ultra-compact silicon photonic integrated interferometer for swept-source optical coherence tomography," Opt. Lett. **39**(17), 5228–5231 (2014).
15. B. I. Akca, C. R. Doerr, G. Sengo, K. Wörhoff, M. Pollnau, and R. M. de Ridder, "Broad-spectral-range synchronized flat-top arrayed-waveguide grating applied in a 225-channel cascaded spectrometer," Opt. Express **20**(16), 18313–18318 (2012).
16. Y. Huang, K. Zhang, J. U. Kang, D. Calogero, R. H. James, and I. K. Ilev, "Noncontact common-path Fourier domain optical coherence tomography method for in vitro intraocular lens power measurement," J. Biomed. Opt. **16**(12), 126005 (2011).
17. U. Sharma, N. M. Fried, and J. U. Kang, "All-fiber common-path optical coherence tomography: sensitivity optimization and system analysis," IEEE J. Sel. Top. Quantum Electron. **11**(4), 799–805 (2005).
18. A. B. Vakhtin, D. J. Kane, W. R. Wood, and K. A. Peterson, "Common-path interferometer for frequency-domain optical coherence tomography," Appl. Opt. **42**(34), 6953–6958 (2003).
19. M. Zhao, Y. Huang, and J. U. Kang, "Sapphire ball lens-based fiber probe for common-path optical coherence tomography and its applications in corneal and retinal imaging," Opt. Lett. **37**(23), 4835–4837 (2012).
20. L. Chang, M. Dijkstra, N. Ismail, M. Pollnau, R. M. de Ridder, K. Wörhoff, V. Subramaniam, and J. S. Kanger, "Waveguide-coupled micro-ball lens array suitable for mass fabrication," Opt. Express **23**(17), 22414–22423 (2015).
21. K. Wörhoff, P. V. Lambek, and A. Driessen, "Design, tolerance analysis, and fabrication of silicon oxynitride based planar optical waveguides for communication devices," J. Lightwave Technol. **17**(8), 1401–1407 (1999).
22. W.-P. Huang and C. Xu, "Simulation of three-dimensional optical waveguides by a full-vector beam propagation method," IEEE J. Quantum Electron. **29**(10), 2639–2649 (1993).
23. N. Weiss, T. G. van Leeuwen, and J. Kalkman, "Localized measurement of longitudinal and transverse flow velocities in colloidal suspensions using optical coherence tomography," Phys. Rev. E Stat. Nonlin. Soft Matter Phys. **88**(4), 042312 (2013).
24. B. D. Goldberg, B. J. Vakoc, W. Y. Oh, M. J. Suter, S. Waxman, M. I. Freilich, B. E. Bouma, and G. J. Tearney, "Performance of reduced bit-depth acquisition for optical frequency domain imaging," Opt. Express **17**(19), 16957–16968 (2009).
25. R. Leitgeb, C. Hitzenberger, and A. Fercher, "Performance of Fourier domain vs. time domain optical coherence tomography," Opt. Express **11**(8), 889–894 (2003).
26. S. Yun, G. Tearney, B. Bouma, B. Park, and J. de Boer, "High-speed spectral-domain optical coherence tomography at 1.3 mum wavelength," Opt. Express **11**(26), 3598–3604 (2003).
27. B. I. Akca, "Spectral-domain optical coherence tomography on a silicon chip," Ph.D. thesis (University of Twente, Enschede, The Netherlands, 2012).
28. P. Pintus, F. Di Pasquale, and J. E. Bowers, "Integrated TE and TM optical circulators on ultra-low-loss silicon nitride platform," Opt. Express **21**(4), 5041–5052 (2013).
29. Y. Chen, D. M. de Bruin, C. Kerbage, and J. F. de Boer, "Spectrally balanced detection for optical frequency domain imaging," Opt. Express **15**(25), 16390–16399 (2007).
30. P. J. Shaw and D. J. Rawlins, "The point-spread function of a confocal microscope - its measurement and use in deconvolution of 3-D data," J. Microsc. **163**(2), 151–165 (1991).
31. W. H. Richardson, "Bayesian-based iterative method of image restoration," J. Opt. Soc. Am. **62**(1), 55–59 (1972).
32. J. L. Starck, E. Pantin, and F. Murtagh, "Deconvolution in astronomy: a review," Publ. Astron. Soc. Pac. **114**(800), 1051–1069 (2002).

#261809 Received 28 Mar 2016; revised 1 May 2016; accepted 2 May 2016; published 1 Jun 2016

33. L. B. Lucy, "An iterative technique for the rectification of observed distributions," Astron. J. **79**(6), 745–754 (1974).
34. S. A. Hojjatoleslami, M. R. N. Avanaki, and A. G. Podoleanu, "Image quality improvement in optical coherence tomography using Lucy-Richardson deconvolution algorithm," Appl. Opt. **52**(23), 5663–5670 (2013).

1. Introduction

Optical coherence tomography (OCT) [1] is an optical imaging technique which provides three-dimensional images with micrometer-resolution. OCT imaging of biological tissue has many clinical applications [2, 3]. More recently, OCT has also been increasingly used in industrial applications [4–8]. The state-of-the-art OCT systems are based on Fourier-domain OCT (FD-OCT) [9], which provides a sensitivity advantage over time-domain OCT (TD-OCT) [10]. FD-OCT is performed as either spectral-domain OCT (SD-OCT) with a broad-band light source and a spectrometer or swept-source OCT (SS-OCT) with a narrow-bandwidth frequency-swept light source [2]. FD-OCT systems provide a one-dimensional depth image (known as an A-scan) with a Fourier transform of the measured spectrum. The cross-sectional images (known as B-scans) are commonly measured by scanning the beam over the sample (such as using a galvanometer scanner) [9]. Currently, most of the OCT systems are based on discrete free-space optical components and fibers. The development in integrated optical circuit technology provides the opportunity to develop chip-based OCT systems having the potential for considerable size and cost reduction. Recently, several chip-based FD-OCT systems have been demonstrated. Akca *et al*. demonstrated a SD-OCT with an 2 × 2 splitter and an integrated spectrometer based on silicon oxynitride (SiON) waveguides where the reference arm was not integrated on the chip [11]. Nguyen et al. demonstrated a SS-OCT system with a Si_3N_4 waveguide based interferometer and reference arm [12]. However, the length of their on-chip reference arm was not long enough to compensate the optical path introduced by a galvanometer scanner in the sample arm. Thus, the sample was translated to obtain B-scans. Yurtsever *et al*. demonstrated two different OCT systems [13, 14]. Both systems have a sufficiently long on-chip reference arm to accommodate a galvanometer scanner in the sample arm to obtain B-scans.

In systems with an on-chip reference arm, the dispersion difference between the reference arm and the sample path needs to be compensated using methods that may reduce the attainable axial resolution [14]. The on-chip reference arm has also relatively large dimensions in many OCT chips, especially in low-contrast waveguide technology where the minimum bending radius is the limiting factor for miniaturization. Another common practical challenge in chip-based systems is the design and fabrication of a broad-bandwidth 50/50 coupler to be used in the interferometer, see e.g [15]. Directional couplers are wavelength-dependent devices of which the coupling ratio is strongly dependent on fabrication accuracy, as reported in [12]. Both deficiencies decrease the efficiency of the OCT system. In all of these chip-based OCT studies, external lenses are needed for the optical chip-to-sample coupling. These external elements can be much larger than the chip itself.

In this study we demonstrate a chip-based common-path SS-OCT system that addresses the problems of current designs. Firstly, by using a common-path OCT system we avoid the need of a separate reference arm. Advantages of common-path OCT compared to dual-arm OCT, such as greater ease of alignment, smaller sensitivity to vibration and better stability, have been demonstrated in several free-space-based or fiber-based OCT systems [16–19]. On our chip we exploit the back reflection from the end facet of the waveguide to act as the reference, thus obviating the need for a separate reference arm. This leads to a significantly smaller footprint of each OCT system which could be interesting for chip-based parallel OCT (see the discussions in the section of Conclusions and outlooks). This solution not only saves space on the chip, but also eliminates the decrease of axial resolution caused by dispersion [14]. Secondly, the three ports (the light source, the detector, and the common-path arm) of the chip are connected by a symmetric Y junction. Such junctions are intrinsically wavelength independent and their design and fabrication are less critical than for a directional coupler.

#261809 Received 28 Mar 2016; revised 1 May 2016; accepted 2 May 2016; published 1 Jun 2016

Thirdly, a directly integrated micro-ball lens [20] is positioned at a short distance from the waveguide facet for efficient coupling of the light between the chip and the sample. This micro-ball lens is the key component enabling the common-path configuration. Firstly, the lens significantly reduces the divergence angle of the light exiting from the waveguide, thus improving the lateral resolution and the chip-sample coupling compared to the case without a lens. Secondly, our SS-OCT has a maximum optical depth range of 5.1 mm (measured from the end facet of the waveguide, limited by the laser source and detector-determined spectrum resolution), of which the lens occupies only the first 0.2 mm, thereby leaving sufficient room for the sample.

The introduction of a lens causes additional reflections at the lens surface, which act as additional parasitic reference planes that reduce the image quality. This artifact has also been observed in a fiber-based common-path OCT system with a 500 μm diameter ball lens [19]. In the Appendix we present a mathematical proof that the effect of multiple references can be removed from the OCT image by using a deconvolution method after characterizing these reflections by measuring a mirror sample. We demonstrate the recovery of the image quality by using a deconvolution algorithm which is more generally applicable to other OCT systems suffering from the effects of multiple reference planes.

2. Experimental setup

The key components of the integrated optical circuit are a Y junction (200 μm long, 7 μm wide) and a polymer micro-ball lens (100 μm in diameter). The circuit was fabricated on a silicon substrate with SiON waveguide technology which was developed in the Integrated Optical MicroSystems group at the University of Twente [21]. The waveguide core is a 600 nm thick, 2 μm wide SiON channel embedded in a SiO_2 layer. The refractive index of the SiON and SiO_2 parts are 1.55 and 1.45, respectively, at λ = 1300 nm. The integration of the polymer micro-ball lens with the SiON waveguide chip is based on photolithography and thermal reflow of a photoresist polymer [20].

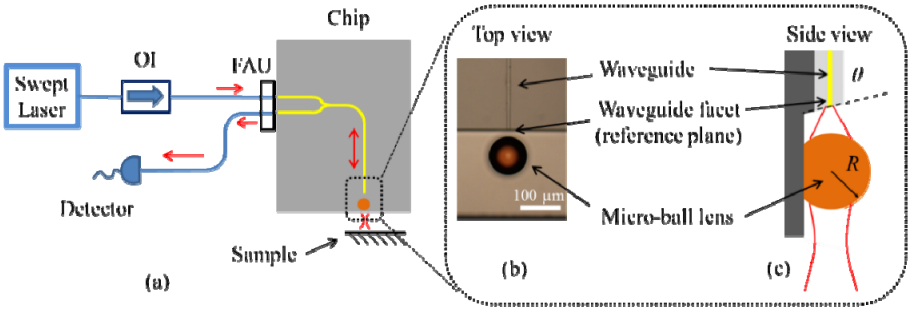

Fig. 1. Schematic of the SS-OCT experimental setup. (a) Light emitted by the swept laser source travels through an optical isolator (OI) and a fiber array unit (FAU) to the chip. The blue lines indicate optical fibers and the yellow lines represent the waveguides on the chip. (b) Microscope image of the end part of the chip showing the channel waveguide and the micro-ball lens. (c) Schematic of the side view of the structure in Fig. 1(b). The end facet is angled at 86 degrees (θ) with respect to the Si substrate plane.

The schematic layout of the SS-OCT system is shown in Fig. 1(a). Light emitted from the swept laser (Axsun Technologies, USA, 1312 nm center wavelength, 92 nm optical bandwidth, 20.9 mW output power, 50 kHz repetition rate) travels through an optical isolator (OI) and is coupled to the chip through a fiber array unit (FAU) with a 250 μm pitch. The splitting ratio of the Y junction has been measured to be between 48/52 and 52/48 in the wavelength range of 1170 nm to 1650 nm by a separate setup. The wavelength range is limited at the short wavelength side by the waveguide becoming multi-modal and at the long wavelength side by the available InGaAs detector. The in-coupled light propagates through

#261809 Received 28 Mar 2016; revised 1 May 2016; accepted 2 May 2016; published 1 Jun 2016

the Y junction with approx. 50% efficiency. The waveguide end facet, which back-reflects part of the light, acts as a reference plane as shown in Figs. 1(b) and Fig. 1(c). Due to the etching process, this facet is angled at 86 degrees (θ) with respect to the substrate plane, as shown in Fig. 1(c). Thus, only 60% (simulated with a beam propagation method [22]) of the Fresnel-reflected light (3.5%) couples to a guided waveguide mode, resulting in a calculated effective power reflection of 2%, which was experimentally verified. The light that is transmitted through the facet travels through the lens onto the sample. For the experiments reported here, we chose a micro-ball-lens arrangement (65 ± 0.5 μm facet-to-lens-center distance, lens radius of 49 ± 0.5 μm) providing the best possible collimated beam (1.6° half divergence angle, 15.3 μm beam waist at 0.3 mm optical path length, corresponding to an expected FWHM lateral resolution of 18 μm, 29 μm, 57 μm and 150 μm at 0.3 mm, 1 mm 2 mm and 5 mm optical path length, respectively) that has been reported in our earlier paper [20] (the beam divergence experiments, in our earlier paper, are repeated at a wavelength of 1.3 μm). Part of the light back-reflected from the sample is coupled into the waveguide through the lens and interferes with the light that is reflected by the end facet. This interference signal propagates through the Y junction where approx. 50% enters into the detection branch. The output signal from the chip is coupled to a detector (Thorlabs PDB 450C, USA; only one port of this balanced photodetector is used) through the same FAU. More details about the used light source and detector configurations can be found in [23].

3. Experimental results and discussion

As the presence of the integrated lens has been shown to provide a considerable reduction of beam divergence [20], a substantial increase of the OCT signal is expected. This improvement is quantitatively demonstrated in Section 3.1. In addition, this measured performance is compared to the theoretical performance expected from the application of a perfect lens which provides a hypothetical 0° divergence beam.

In Section 3.2 we present a comprehensive noise analysis covering three operating regimes for reflected reference power P_R and reflected sample power P_S, viz. $P_R >> P_S$, $P_R \approx P_S$, and $P_R << P_S$. In most OCT studies involving biological samples the reflected sample power has been assumed to be much smaller than the reflected reference power [10, 24, 25] because the back-scattered power fraction from a typical biological sample is on the order of 10^{-5} [2]. Therefore, the noise of the system is dominated by the noise in the reflected reference power, hence independent of the sample. However, OCT is also increasingly used in industrial applications [4–7] where the reflectivity of the sample (such as the internal wall surface of an electronic panel [4]) could be close to one. Thus the condition of $P_R >> P_S$ is not always satisfied in case of a strongly reflecting sample.

In Section 3.3 the performance of our chip system is compared with that of a fiber system, and potential improvements of the chip system are discussed.

In Section 3.4 we show cross-sectional images of an optical phantom sample, which were obtained with our integrated probe. Some ghost images were noticed, which are caused by closely spaced (less than the coherence length of a spectral channel) multiple reference reflections from the waveguide end facet and the lens surface. A method is demonstrated that largely removes these ghost images.

The mathematical details of this method, which is based on a model of a multiple reference in FD-OCT, is presented in the Appendix. The method is applicable to both SS-CT and SD-OCT.

3.1 Signal enhancement with a micro-ball lens

The optical power levels were measured at several positions in the optical setup without and with a microlens (Table 1). These optical power levels are important to quantitatively understand the signal enhancement realized with the micro-ball lens and the noise analysis.

#261809 Received 28 Mar 2016; revised 1 May 2016; accepted 2 May 2016; published 1 Jun 2016

The laser power (9 ± 0.2 mW before coupling to the chip) was the same for all measurements in Table 1. A mirror sample was located as close as possible to the chip, which is approx. 0.1 mm distance, resulting in 0.3 mm and 0.1 mm optical path length from the sample to the waveguide facet in the case with and without a lens, respectively. The reflected reference power P_R and reflected sample power P_S were both measured at the detector location as shown in Fig. 1(a). The power incident on the sample is measured by placing a power meter at the position of the mirror sample. The irradiance at the sample is estimated using the beam radius (23.6 ± 0.5 μm without lens, 15.3 ± 0.5 μm with lens) at the sample position.

The results in Table 1 show that P_R, P_I, and the irradiance at the sample are similar in both systems. The slightly larger P_R and slightly smaller P_I in the situation with a micro-ball lens are due to reflections from the surfaces of the lens. Despite the larger optical path length between sample and waveguide facet P_S is approximately 100 times larger with compared to without the lens. P_R and P_I are kept the same as in Table 1 for all the OCT measurements with the chip system in this study. P_S and the irradiance at the sample are different for different optical path lengths. P_S decreases rapidly in case of no lens, such that it cannot be measured directly (with the current setup) at larger optical path lengths but can only be calculated from the OCT measurements.

Table 1. Measured Reflected Reference Power, Reflected Sample Power and Power Incident on the Sample with and without a Micro-ball Lens

	Reflected reference power P_R (μW)	Reflected sample power P_S (μW)	Power incident on the sample P_I (mW)	Peak irradiance (Gaussian beam) at the sample (W/cm^2)
Without micro-ball lens	12.0 ± 0.5	2.8 ± 0.5	2.9 ± 0.1	(3.3 ± 0.3) × 10^2
With a micro-ball lens	14.5 ± 0.5	(2.9 ± 0.1) × 10^2	2.6 ± 0.1	(7.1 ± 0.5) × 10^2

In order to study the OCT signal enhancement with the lens, the A-scan results of a mirror sample measured with and without the lens are shown in Fig. 2(a). A peak is clearly visible at a position that corresponds to the optical path length between the mirror sample and the end-facet of the waveguide. For this measurement, the sample has been located at approximately 0.33 mm and 0.36 mm from the waveguide facet in the respective cases with and without lens; the small offset was introduced to distinguish both peaks in the same graph. This means that in the case without the lens, the P_S and peak irradiance at the sample were different from those listed in Table 1. The signal peak magnitude as measured for the chip with the micro-ball lens is a factor of 28 larger than the one measured without a lens. The peak magnitude is given by

$$A_{magnitude} \propto M \rho \sqrt{P_R P_S}\, \tau_i, \tag{1}$$

where M = 1088 is the total number of spectral channels, ρ = 1 A/W is the average responsivity of the detector, and τ_i = 13.4 ns is the average integration time of each spectral channel [2]. This means that the collected reflected sample power P_S is approximately 780-fold enhanced by the micro-ball lens. This enhancement can be different for other optical path lengths and scattering properties of the sample. The FWHM of the signal peak is measured to be 11.8 ± 0.2 μm in both cases, which is almost identical with the fiber-based system as shown in Table 2.

The OCT signal roll-off (measured as the peak magnitude in the A-scan as a function of optical path length) with and without a micro-ball lens is compared in Fig. 2(b). For these measurements the mirror sample was positioned at different distances from the waveguide facet, with the same light source and detector settings in all cases. The presence of the micro-ball lens enhances the signal strength by up to 37 dB depending on the optical path length. In

#261809 Received 28 Mar 2016; revised 1 May 2016; accepted 2 May 2016; published 1 Jun 2016

the same figure, the calculated expected signal roll-off is presented, following Eq. (2) in the paper of Yun [26]. For comparison, the calculated signal is normalized to the largest signal measured with a micro-ball lens. The calculated signal roll-off is based on the finite spectral resolution of the system, assuming a constant chip-sample coupling efficiency over the whole optical path length range. The values used in this calculation are 5.1 mm maximum optical path length and the ratio 0.73 of the spectral resolution to the sampling interval which is approximated by the detector duty cycle (0.73).

From Fig. 2(b) it follows that the micro-ball lens extends the 6 dB roll-off range from 0.2 ± 0.1 mm to 1.7 ± 0.1 mm. This 6 dB roll-off range is commonly used as a characteristic parameter to indicate the signal decreasing speed of an OCT system. Since we could not measure the sample signal at exactly zero optical path length in our common-path configuration, the 6 dB signal roll-off is referred to the closest point (first point) measured in each system. The faster signal roll-off in the experiment, compared to the calculated one (which assumes a hypothetical 0° divergence beam), is most likely caused by the decrease of the chip-sample coupling efficiency due to the beam divergence.

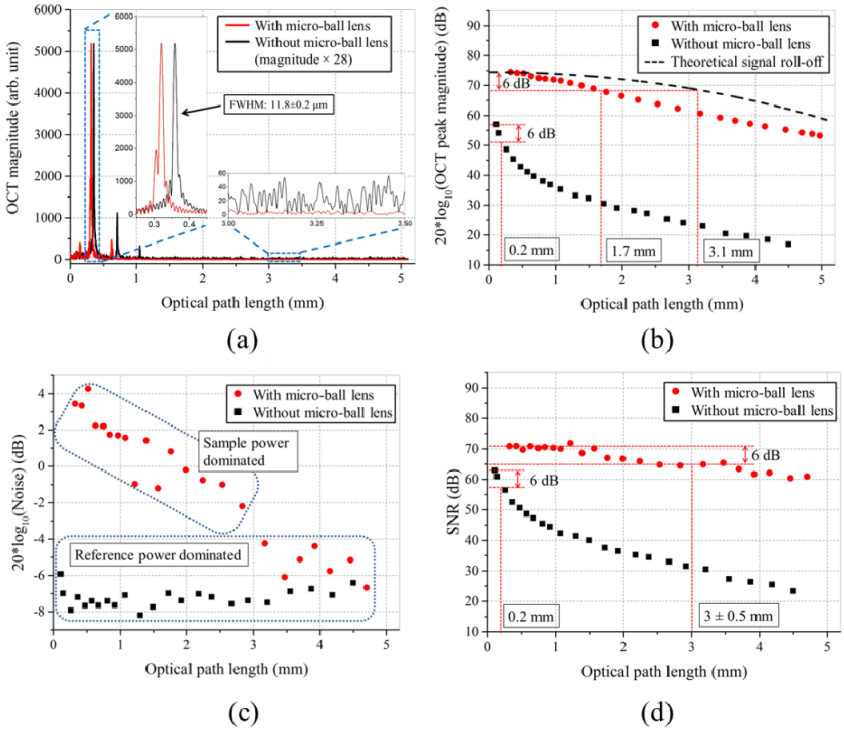

Fig. 2. Characterization of the chip-based OCT system. (a) A-scan results of a mirror sample measured with and without a micro-ball lens. The signal measured without the lens is multiplied by 28 to obtain equal peak magnitude for the cases with and without lens to enable easy comparison. The insets show a zoom in to the main signal peak and the noise floor, respectively. (b) Signal roll-off measured with and without a micro-ball lens. The peak position of each A-scan is marked with a red dot for the case with a lens and a black square for the case without lens. The peak magnitude is given in dB units, where 0 dB corresponds to the value 1 of the arbitrary unit used in Fig. 2(a). The dashed black curve is a calculated signal roll-off based on the finite spectral resolution of the system. The red dashed lines indicate the 6 dB roll-off optical path length for each curve. (c) Measured noise as a function of optical path length. The measurements are categorized into two groups, namely sample power dominated and reference power dominated. (d) SNR roll-off comparison between chips with and without a lens. The red dashed lines indicate the 6 dB roll-off optical path length of each curve. The SNR roll-off curve in the case with a lens is rather flat, leads to a large uncertainty (± 0.5 mm) in the 6 dB roll-off range.

#261809 Received 28 Mar 2016; revised 1 May 2016; accepted 2 May 2016; published 1 Jun 2016

3.2 Noise and signal-to-noise ratio (SNR)

The noise in an OCT measurement, specified as the standard deviation σ of the signal fluctuations, measured at the noise floor of an A-scan, is given by

$$\sigma_{measured} = \sqrt{\sigma_{read}^2 + \sigma_{shot}^2(P) + \sigma_{RIN}^2(P)}, \quad (2)$$

where σ_{read}, σ_{shot}, and σ_{RIN} denote read-out noise, shot noise, and relative intensity noise (RIN), respectively, and $P = P_R + P_S$ is the total power on the detector. For given detector settings, σ_{read} does not depend on the signal. Shot noise and RIN have power dependencies of $\sigma_{shot}(P) \propto \sqrt{P}$ and $\sigma_{RIN}(P) \propto P$, respectively [24].

The total noise, $\sigma_{measured}$, measured as a function of the sample optical path length for the chip system, both with and without a lens is shown in Fig. 2(c). The noise is given in the same dB units as the signal in Fig. 2(b), i.e., $20\log_{10}(\text{Noise})$. The noise stays constant with increasing optical path length in the chip system without a lens. The noise decreases with increasing optical path length in the chip system with a lens.

In both systems, the reference power is kept constant (12.0 μW without a lens and 14.5 μW with a lens as shown in Table 1), and the sample power decreases with increasing optical path length. From the measured power data in Table 1, it can be seen that $P_R >> P_S$ in the case without a lens. So the noise is dominated by the noise level of the reference power, where $\sigma_{measured} \approx \sqrt{\sigma_{read}^2 + \sigma_{shot}^2(P_R) + \sigma_{RIN}^2(P_R)}$ from Eq. (2) is a constant. This explains the constant noise level in the chip system without a lens.

The ratio of reflected sample power to reference power in the chip system with a lens can be calculated using Eq. (1), Fig. 2(b), and Table 1. The result is that the reflected sample power is a factor of 20 larger than the reference power ($P_R << P_S$) for a mirror-to-chip distance of 0.3 mm, and decreases to 20% of the reference power ($P_R >> P_S$) at a distance of 4.7 mm. At 3 mm optical path length, the reflected sample power is about the same as the reference power ($P_R \approx P_S$). Therefore, the noise of the chip with a lens can be classified in two different regimes, as indicated in Fig. 2(c), namely the sample-power-dominated and the reference-power-dominated regimes.

In the measurements discussed above, the sample was a mirror causing a relatively high reflected sample power due to its high reflection coefficient. This condition is relevant in case of certain industrial applications where highly reflective surfaces are measured [4]. In case of biological applications, the tissue will produce considerably less sample power ($P_R >> P_S$), so that all measurements in this case would be performed in the reference-power-dominated regime with an approximately constant noise level. For any other partially reflecting samples [5–7], the noise in the chip system with a lens should fall in the region between the red dots and black squares indicated in Fig. 2(c).

The SNR is calculated as $20\log_{10}(\text{OCT peak magnitude}/\text{noise})$. The SNR roll-off with optical path length is shown in Fig. 2(d). The 6-dB SNR roll-off optical path length of the chip without a lens is 0.2 ± 0.1 mm, which is the same as its signal roll-off. However, the 6-dB SNR roll-off optical path length of the chip with a lens, in the sample-power-dominated regime, is 3.0 ± 0.5 mm which is much larger than its signal roll-off (1.7 ± 0.1 mm). This extended roll-off optical path length is due to the fact that the noise is decreasing with increasing optical path length as shown in Fig. 2(c).

The signal roll-off curve [Fig. 2(b)] and the SNR roll-off curve [Fig. 2(d)] together set the boundary of roll-off rate in the SNR for different samples. The SNR roll-off curve in Fig. 2(d) is measured with a mirror which has the largest sample power noise. This leads to the fastest

#261809 Received 28 Mar 2016; revised 1 May 2016; accepted 2 May 2016; published 1 Jun 2016

decrease in the noise with sample power, thus the slowest decrease in the SNR. In the case of a weakly scattering sample, the noise will be dominated by a constant reference power noise, thus the SNR decreases at the same rate as the signal. For any other samples, the SNR roll-off is slower than the signal roll-off and faster than the SNR roll-off measured with a mirror. Thus the 6 dB SNR roll-off optical path length of any sample should be between 1.7 ± 0.1 mm and 3.0 ± 0.5 mm for the chip with a lens. For a weakly scattering tissue sample, the 6-dB SNR roll-off optical path length should be 1.7 ± 0.1 mm (the same as the signal roll-off).

3.3 Performance comparison with a fiber system

The performance of the chip system having a lens is compared to that of a bulk fiber SS-OCT system [23], using exactly the same light source and photodetector. The following conditions were kept constant in the experiments:

(a) Settings of the swept laser source and the detector.

(b) Reflected reference power, P_R = 14.5 ± 1 μW, in the absence of the sample.

(c) Power incident on the sample P_I = 2.6 ± 0.1 mW.

(d) Mirror sample placed at approx. 0.3 mm (optical path length) distance from the reference plane (the waveguide facet in case of the chip system).

The key parameters in the corresponding A-scans of both systems are listed in Table 2.

Table 2. Comparison of Measured A-scan Parameters between the Chip System and a Fiber System

	Signal peak (arb. units)	FWHM (μm)	Noise (arb. units)	SNR (dB)
Chip with micro-ball lens	$(5.2 \pm 0.1) \times 10^3$	11.8 ± 0.2	1.5 ± 0.1	71 ± 1
Fiber system	$(15.8 \pm 0.1) \times 10^3$	12.5 ± 0.2	1.2 ± 0.1	82 ± 1

The OCT signal peak magnitude of the chip system is approximately one third of that of the fiber system and the FWHM of the signal peaks in both systems are almost identical. The smaller signal peak magnitude in the chip system is caused by the larger optical losses compared to the fiber system. The power transmittance from the sample to the detector in the fiber system is measured to be 54 ± 2% at this optical path length. This is mainly limited by the coupling efficiency of the bulk lens used in this fiber system. Based on Eq. (1), the chip system should have approx. 9 times smaller transmittance (~6%) in the same path than in the fiber system. The power transmittance of every component from sample to detector in the chip system is as follows:

1. The micro-ball lens has a measured power transmittance of 89 ± 2% due to Fresnel reflection.
2. The coupling from the micro-ball lens to the waveguide is 48 ± 5%, which is calculated based on the measured total transmittance at this optical path length and transmittance of every other components. This coupling efficiency is similar to that of the bulk lens used in the fiber system.
3. The propagation losses of the waveguide (0.1 dB/cm [27]) lead to a transmittance of 91 ± 2%.
4. The on-chip Y junction has a transmittance into the detector arm of 49 ± 2%.
5. The coupling from the chip to the detector is 59 ± 2% due to the mode mismatch between waveguide and fiber.

Therefore, the total transmittance of the chip system from the sample to the detector is 11 ± 2%, which is not around 6% as calculated with Eq. (1). This mismatch is due to the fact that the reflected reference power, 14.5 μW, in case of the chip system is the sum of the

#261809 Received 28 Mar 2016; revised 1 May 2016; accepted 2 May 2016; published 1 Jun 2016

contributions from three references as will be discussed in Section 3.4. The reference power that contributes to the main signal peak is only 11.5 ± 1 μW rather than 14.5 ± 1 μW, which explains the mismatch within the experiment error.

The power transmittance in the chip system can be improved in the following ways.

1. An anti-reflection coating on the lens could reduce the Fresnel reflection.
2. The sample-chip coupling can be improved by using a larger diameter micro-ball lens which can provide a beam with a Rayleigh range covering the entire range of interest.
3. Using shorter waveguides (from currently 4 cm to a few 100 μm) to connect the ports of the Y junction will lead to smaller propagation losses.
4. Using an on-chip low-loss circulator instead of the Y junction will eliminate its intrinsic 50% loss. However, the design and fabrication of such a circulator is rather challenging, especially for a broad wavelength range [28].
5. The fiber-chip coupling could be improved by designing a suitable waveguide taper.

Despite the larger signal peak, resulting in an expected larger shot noise, the measured noise is slightly smaller for the fiber system (see Table 2). The reason is that the fiber system uses a separate reference path, enabling the application of a balanced detector. This significantly reduces the RIN arising from the laser power fluctuation [29]. Thus, the total noise in the fiber system is smaller than in the chip system. One possible solution to reduce the RIN noise in the chip system is to monitor the laser power and apply post processing by software.

3.4 Multiple reference planes and phantom imaging

Close inspection of Fig. 2(a) shows the appearance of relatively strong shoulders on the main peak for the case when the micro-ball lens is used. This is caused by Fresnel reflections that take place, not only at the end facet of the waveguide (the intended reference plane), but also from the front and back surfaces of the micro-ball lens. These lens surfaces, therefore, act as two additional reference planes in this common-path OCT system. Next, we will demonstrate that using a deconvolution technique the artefacts in the A-scan caused by the lens can be eliminated. A mathematical model of a multiple-reference FD-OCT system is described in the Appendix. A main result in the Appendix is Eq. (18), which is given here in a simplified form,

$$i_{D,image}(z) = G \otimes H_{PSF}, \tag{3}$$

where ⊗ denotes convolution, G and H_{PSF} are functions of wavenumber, G contains the sample information, and H_{PSF} is the point spread function (PSF) [30] of the OCT system in the axial direction, which is independent of the sample. The PSF is composed of the broadening function depending on the source bandwidth, and a function describing the dependence on the reflectivities and relative positions of the reference planes. This PSF can be characterized by measuring the response of a well-known sample (a mirror) as indicated in the Appendix. In case of a multiple references OCT like in our chip system, this PSF is a multi-peak function resulting in ghost images for every additional reference plane that may overlap with the image that originates from the primary reference plane. A commonly used imaging processing technique, deconvolution, can be used to suppress or remove these unwanted ghost images [30].

Here we investigate the applicability of the deconvolution technique for suppressing the ghost images. To this end, the PSF of our chip system is measured with a mirror sample, since G is a delta function in the case of a mirror sample. A zoomed-in view of an A-scan result of a mirror sample is shown by the black curve in Fig. 3(a), which is the PSF of our system. The

#261809 Received 28 Mar 2016; revised 1 May 2016; accepted 2 May 2016; published 1 Jun 2016

effect of the two additional references is clearly visible as two additional peaks (peak 2 and 3) in Fig. 3(a). The peaks 1, 2 and 3 in Fig. 3(a) are the interference of the mirror-waveguide-facet, mirror-lens-surface (close to the waveguide) and mirror-lens-surface (far from the waveguide), respectively. Next, this PSF is used in the deconvolution of A-scans from any sample measured with this chip system. An example of a deconvolution result is shown with the red curve in Fig. 3(a) which shows a strong suppression of the peaks caused by reflections from the lens' surfaces.

In theory, the measurement of the H_{PSF} is not sensitive to the position of the mirror sample with respect to the reference planes. Several PSF measurement using different mirror distances have been performed and no significant differences were observed in the results.

Finally, we apply our OCT system to an optical phantom. The optical phantom that is used consists of three scattering layers separated by two transparent layers. The scattering layer, used to mimic the skin, is silicone elastomer-based which includes scattering by adding TiO_2 or SiO_2 particles [31]. This layered sample is placed on a glass slide which is mounted on a translation stage to obtain B-scans. Two zoomed-in cross-sectional imagines (B-scan) are shown in Fig. 3(b) and Fig. 3(c). Each A-scan in the B-scan is averaged over 30 measurements. The image after deconvolution shows a clear improvement in the contrast. This is due to the suppression of the ghost images of the scattering layers.

The full range of a deconvolved B-scan is shown in Fig. 3(d). The two lines that show up close to zero optical path length are caused by the reflections of the micro-ball lens surface. Although a background measurement without the sample has been subtracted from the sample measurement to remove these reflection lines. The coupling efficiency between the fiber and chip varies from measurement to measurement due to mechanical instability of our experimental set-up, which leads to a small power difference in these reflections. This small power difference results in incomplete cancellation of these two reflections. This problem is unimportant because these artifacts are always at the same location and are distinct from the sample image. It can be largely solved by gluing the FAU to the chip, which will remove the coupling uncertainty between measurements.

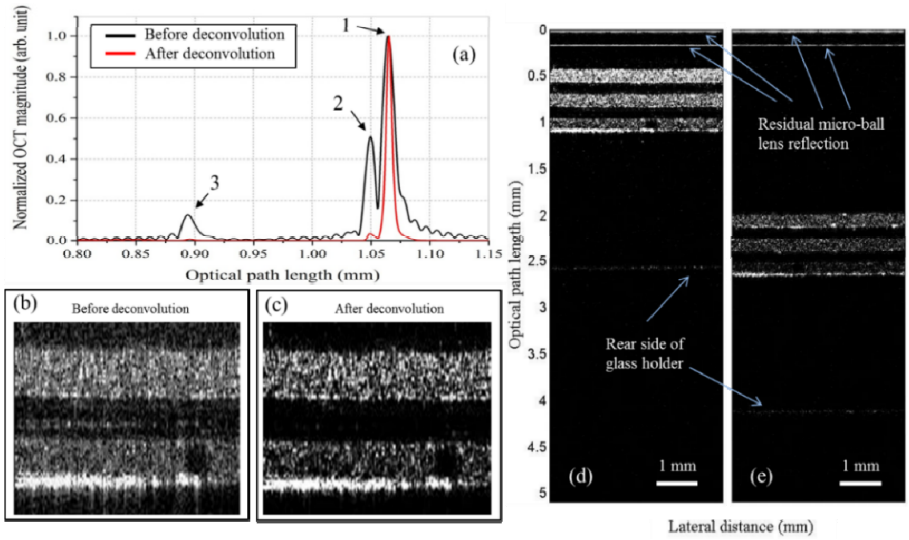

Fig. 3. (a) A zoomed-in view of an A-scan result of a mirror sample. This plot shows the effect of multiple references on a mirror sample (black curve) and its deconvolved solution (red curve). (b) and (c) Zoomed in cross-sectional images of a phantom sample before and after deconvolution. (d) and (e) The deconvolved phantom images at different distances from the chip.

#261809 Received 28 Mar 2016; revised 1 May 2016; accepted 2 May 2016; published 1 Jun 2016

The image in Fig. 3(e) is a deconvolved B-scan of the phantom measured at a larger distance from the chip. The image of the phantom becomes dimmer with increasing optical path length. Scattering layers are still clearly visible at an optical path length of 2.6 mm. Scattering (the glass holder and the sample were placed under angle to avoid specular reflection) from the rear side of the glass holder is even visible up to 4.2 mm.

Many different deconvolution algorithms exist for image processing. The deconvolution result may be different depending on the noise in the measurement and the algorithm used [32]. Since the described experiment is intended as a proof of concept that the artefacts arising from the multiple reference planes can be suppressed with a deconvolution approach, we did not perform a systematic study of different deconvolution algorithms. A further study on the selection of the deconvolution algorithms may be needed to find the optimal algorithm for this particular system.

The B-scans demonstrated here were obtained by translating the sample. Since the micro-ball lens is integrated and the optical chip is a small low-mass device, an alternative implementation might mount the fiber-connected chip directly on a scanner to obtain two- or three-dimensional images.

4. Conclusions and outlooks

In this study, we have demonstrated a chip-based common-path SS-OCT system with an integrated micro-ball lens. The common-path design eliminates the space-consuming and dispersive on-chip loop reference arm. Therefore, no dispersion compensation is needed to achieve the light-source-limited axial resolution. The three-port configuration (light source, common-path arm, and detector) enables the use of a wavelength-independent 50/50 Y junction which is much less sensitive to fabrication errors compared to a directional coupler. The drawbacks of this common-path configuration is that it cannot use a balanced detector, which leads to around 3–4 dB lower sensitivity compared to a traditional dual-arm OCT [19]. The use of an on-chip micro-ball lens eliminates the need for external optical elements for coupling the light between the chip and the sample. Such a micro-ball lens enables a very short distance of a few hundred μm between the sample and the reference plane, which is an important requirement for common-path OCT. The use of this micro-ball lens leads to a signal enhancement up to 37 dB compared to the chip without a lens, for a mirror sample. A multiple-reference FD-OCT model has been developed. Multiple ghost images caused by additional reference planes (originating from the lens surface) could be largely suppressed using a deconvolution scheme. Finally, cross-sectional imaging of a layered optical phantom, with suppressed ghost image, has been demonstrated.

The minimum footprint of this design could, in principle, be as small as ~400 × 100 μm, which may enable the fabrication of a chip-based parallel OCT system with multiple independent detection channels. The minimum length of ~400 μm is determined from the 200-μm long Y junction plus the 100-μm diameter micro-ball lens, plus some spacing. (However, in order to facilitate testing of the device, our prototype was equipped with several cm long straight access waveguides.) The minimum width of ~100 μm is determined from the diameter of the lens.

We believe that, by integrating a micro-ball lens onto the chip and using a common-path configuration, we have moved a significant step forward in the development of on-chip SS-OCT systems.

Appendix

Here, we present a model, extended from the model in [2], for a FD-OCT with multiple reference planes. This model mathematically proves that the multiple references lead to a convolution effect in an OCT A-scan. A mirror sample can be used to measure the transfer function and deconvolve any other A-scan to recover the original sample image.

#261809 Received 28 Mar 2016; revised 1 May 2016; accepted 2 May 2016; published 1 Jun 2016

Assume the light source provides a polychromatic plane wave of which the electric field is expressed in complex form as

$$E_i = s(k)e^{i(kz-\omega t)}, \tag{4}$$

where ω is the angular frequency, t is the time, k is the wavenumber, z is the optical distance from the source along the optical axis, and $s(k)$ is the amplitude spectral density of the electric field.

The field transmission coefficient from the light source to the sample is t_{LS} and from the sample to the detector is t_{SD}. If the sample is modeled as a set of N discrete partial reflectors with respective effective field reflection coefficients r_{Sn}, which incorporate the depth-dependent absorption and scattering losses in the sample, the field E_S incident on the detector after returning from the sample, in absence of the reference arm, can be expressed as

$$E_S = E_i t_{LS} t_{SD} e^{ikz_D} \sum_{n=1}^{N} \left(r_{Sn} e^{2ikz_{Sn}} \right), \tag{5}$$

where z_D is the optical distance from the main reference plane, which is the waveguide end facet, to the detector, and z_{Sn} is the optical distance from the facet to the n^{th} reflector in the sample.

The field transmission coefficient from the light source to the reference plane is t_{LR} and that from the reference plane to the detector is t_{RD}. Assume J discrete planes with effective reflection coefficients r_{Rj} (defined similar to the assumed discrete 'sample reflectors' r_{Sn}). The field incident on the detector after returning from the reference in the absence of the sample arm is

$$E_R = E_i t_{LR} t_{RD} e^{ikz_D} \sum_{j=1}^{J} \left(r_{Rj} e^{2ikz_{Rj}} \right), \tag{6}$$

where z_{Rj} is the optical distance from the facet to the j^{th} reference plane. Multiple reflections between these planes are considered as separate planes at different (longer) optical distances.

The waves returning from reference and sample interfere at the detector. The photocurrent generated by the detector is proportional to the square of the sum of the fields incident upon it, as given by

$$I_D(k) = \rho(k) \left\langle c\varepsilon_0 A \left| E_R + E_S \right|^2 \right\rangle. \tag{7}$$

Here, $\rho(k)$ is the responsivity of the detector as a function of wavenumber (units Amperes/Watt), the angular brackets denote the (time) average over the response time of the detector, c is the speed of light, ε_0 is the vacuum permittivity and A is the cross-sectional area of the light beam (assuming the detection area is larger than the beam). Equation (4)-(6) are substituted into Eq. (7) and the location z of the main reference plane (the facet) is chosen to be $z = -z_D$ for convenience. As the period of the source optical wave is much smaller than the detector response time, and the system is assumed to be stationary, this leaves the temporally invariant terms

#261809 Received 28 Mar 2016; revised 1 May 2016; accepted 2 May 2016; published 1 Jun 2016

$$I_D(k) = \rho(k)S(k)\left[T_{LR}T_{RD}(R_{R1}+R_{R2}+\ldots)+T_{LS}T_{SD}\left(R_{S1}+R_{S2}+\ldots\right)\right]$$

'Direct current (DC) terms'

$$+\rho(k)S(k)\sqrt{T_{LR}T_{RD}T_{LS}T_{SD}}\sum_{j=1}^{J}\sum_{n=1}^{N}\left\{\sqrt{R_{Rj}R_{Sn}}\left[e^{i2k\left(z_{Sn}-z_{Rj}\right)}+e^{-i2k\left(z_{Sn}-z_{Rj}\right)}\right]\right\}$$

'Cross-correlation terms'

$$+\frac{1}{2}\rho(k)S(k)T_{LR}T_{RD}\sum_{\substack{j=1\\j\neq h}}^{J}\sum_{h=1}^{J}\left\{\sqrt{R_{Rj}R_{Rh}}\left[e^{i2k\left(z_{Rj}-z_{Rh}\right)}+e^{-i2k\left(z_{Rj}-z_{Rh}\right)}\right]\right\} \tag{8}$$

'Auto-correlation terms of reference'

$$+\frac{1}{2}\rho(k)S(k)T_{LS}T_{SD}\sum_{\substack{n=1\\n\neq m}}^{N}\sum_{m=1}^{N}\left\{\sqrt{R_{Sn}R_{Sm}}\left[e^{i2k(z_{Sn}-z_{Sm})}+e^{-i2k(z_{Sn}-z_{Sm})}\right]\right\}$$

'Auto-correlation terms of sample'.

here,

$$S(k)=\frac{1}{2}c\varepsilon_0 A\left|s(k)\right|^2 \tag{9}$$

is the power spectral density of the light source, and

$$T_{LR}=\left|t_{LR}\right|^2, T_{RD}=\left|t_{RD}\right|^2, T_{LS}=\left|t_{LS}\right|^2, T_{SD}=\left|t_{SD}\right|^2, R_{Rj}=\left|r_{Rj}\right|^2, \text{and } R_{Sn}=\left|r_{Sn}\right|^2 \tag{10}$$

are the optical power transmittance and reflectance. The factor 1/2 in the "auto-correlation" terms is a result of the double counting of $n = a$ and $m = b$ with the identical contributions of $n = b$ and $m = a$. The cross-correlation terms and auto-correlation terms of the sample are the parts containing the sample information of interest. For a weakly scattering biological sample (reflectivity on the order of ~10^{-4} to 10^{-5}), the auto-correlation terms of the sample are normally negligible compared to the cross-correlation terms [2]. The first half of the DC terms, and the auto-correlation terms of the reference are independent of the sample. Therefore, they can be considered as a background and obtained by a measurement without any sample. This background then can be subtracted in subsequent sample measurements. The remaining parts are the second half of the DC terms and the cross-correlation terms, which are well separable in an A-scan due to their different z-positions.

Assuming that all reference planes have a fixed reflectivity and location in the system, we can write

$$z_{R2}=z_{R1}+\Delta z_{21}, z_{R3}=z_{R1}+\Delta z_{31},\ldots, \tag{11}$$

where Δz_{j1} is the optical distance of the j^{th} reference plane to the first (main) reference plane. Then the cross-correlation terms in $I_{Dc}(k)$ can be written as

#261809 Received 28 Mar 2016; revised 1 May 2016; accepted 2 May 2016; published 1 Jun 2016

$$
\begin{aligned}
I_{D,cross}(k) = \rho(k)S(k)\left[c_{SR1}(k) + c_{SR1}(k)^*\right] \\
\text{'from reference plane 1'} \\
+\rho(k)S(k)\left[\frac{\sqrt{R_{R2}}}{\sqrt{R_{R1}}}c_{SR1}(k)e^{-i2k\Delta z_{21}} + \frac{\sqrt{R_{R2}}}{\sqrt{R_{R1}}}c_{SR1}(k)^* e^{i2k\Delta z_{21}}\right] \\
\text{'from reference plane 2'} \\
+\rho(k)S(k)\left[\frac{\sqrt{R_{R3}}}{\sqrt{R_{R1}}}c_{SR1}(k)e^{-i2k\Delta z_{31}} + \frac{\sqrt{R_{R3}}}{\sqrt{R_{R1}}}c_{SR1}(k)^* e^{i2k\Delta z_{31}}\right] \\
\text{'from reference plane 3',}
\end{aligned}
\tag{12}
$$

where * denotes the complex conjugate and

$$
c_{SR1}(k) = \sqrt{T_{LR}T_{RD}T_{LS}T_{SD}}\sum_{n=1}^{N}\left\{\sqrt{R_{R1}R_{Sn}}e^{i2k(z_{Sn}-z_{R1})}\right\}. \tag{13}
$$

The first line in Eq.(12) is the signal caused by the reference plane 1, which is identical to the signal of a single-reference OCT system. The corresponding A-scan from reference 1 (excluding the DC terms) is

$$
i_{D,\text{cross},R1,image}(z) = F\left[\rho(k)S(k)c_{SR1}(k)\right] = F\left[\rho(k)S(k)\right] \otimes F\left[c_{SR1}(k)\right], \tag{14}
$$

and its mirrored artifact is

$$
i_{D,\text{cross},R1,\text{artifact}}(z) = F\left[\rho(k)S(k)c_{SR1}(k)^*\right] = F\left[\rho(k)S(k)\right] \otimes F\left[c_{SR1}(k)^*\right], \tag{15}
$$

where $F[\ ]$ denotes the Fourier transform and $\otimes$ denotes convolution. Equation (14) indicates that even for a normal single-reference plane OCT, the A-scan can be understood as an infinity sharp sample function $F\left[c_{SR1}(k)\right]$ convolved with a light source and detector bandwidth limited broadening function $F\left[\rho(k)S(k)\right]$.

The complete cross-correlation terms can be further expressed as

$$
I_{D,cross}(k) = \rho(k)S(k)\left[c_{SR1}(k)\alpha(k) + c_{SR1}(k)^*\alpha(k)^*\right], \tag{16}
$$

where

$$
\alpha(k) = \left(1 + \sum_{j=2}^{J}\frac{\sqrt{R_{Rj}}}{\sqrt{R_{R1}}}e^{-i2k\Delta z_{j1}}\right) \tag{17}
$$

describes the influence of the reference planes on the signal. In case of a single reference system (J = 1), the summation term in Eq. (17) is zero, thus $\alpha(k)$ = 1. In case of a multiple reference system, the summation term in Eq. (17) indicates the reflectance (R_{Rj}) and distance (Δz_{j1}) relation of all the reference planes (R_j) to the first reference plane (R_1).

The A-scan (excluding the DC terms) from this multiple-reference OCT is

$$
\begin{aligned}
i_{D,cross,image}(z) &= i_{D,\text{cross},R1,image}(z) \otimes F\left[\alpha(k)\right] \\
&= F\left[c_{SR1}(k)\right] \otimes F\left[\rho(k)S(k)\right] \otimes F\left[\alpha(k)\right],
\end{aligned}
\tag{18}
$$

#261809 Received 28 Mar 2016; revised 1 May 2016; accepted 2 May 2016; published 1 Jun 2016

where $F\left[c_{SR1}(k)\right]$ describes the response of the sample, $F\left[\rho(k)S(k)\right]$ is the broadening function caused by the finite bandwidth of the light source and $F\left[\alpha(k)\right]$ is a *J*-peak comb-like function describing the influence of the reference planes on the signal. Thus the point spread function (PSF) of the system in the axial direction is

$$H_{PSF} = F\left[\rho(k)S(k)\right] \otimes F\left[\alpha(k)\right], \tag{19}$$

which is independent of the sample. Overlapping of the sample images will occur if the thickness of the sample is larger than the spacing of the comb peaks in $F\left[\alpha(k)\right]$. However, the overlapped image can be recovered to a certain degree by deconvolution if the PSF is known [30].

This axial direction PSF can be measured as

$$H_{PSF} = i_{D,cross,image}(z) \tag{20}$$

with a mirror sample, since the sample function $F\left[c_{SR1}(k)\right]$ is a Dirac delta function. An example of the measured PSF is shown with the black curve in Fig. 3(a). One of the Matlab deconvolution functions 'deconvlucy' (based on the Richardson–Lucy deconvolution [31, 33], which is a commonly used iterative algorithm in imaging processing [34]) is used on the black curve in Fig. 3(a). The result is shown with the red curve in Fig. 3(a) which shows a strong suppression of the peaks caused by reflections from the lens' surfaces. Deconvolution with this PSF even sharpen the main peak to a certain degree, which may slightly improve the axial resolution of the OCT system.

Acknowledgments

The authors acknowledge support from the IOP Photonic Devices program (Low-cost handheld OCT device, IOP PD100019) managed by the Technology Foundation RVO.

#261809 Received 28 Mar 2016; revised 1 May 2016; accepted 2 May 2016; published 1 Jun 2016